Improving the full quantum eigensolver with exponentiated operators

Bozhi Wang,[1,2] Jingwei Wen,[3] Jiawei Wu,[4] Haonan Xie,[1] Fan Yang,[1,2] Dong Ruan,[1] Shijie Wei,[2,*] and Gui-lu Long[1,2,5,6,†]

[1]*State Key Laboratory of Low-Dimensional Quantum Physics and Department of Physics, Tsinghua University, Beijing 100084, China*

[2]*Beijing Academy of Quantum Information Sciences, Beijing 100193, China*

[3]*China Mobile (Suzhou) Software Technology Company Limited, Suzhou 215163, China*

[4]*Centre for Quantum Technologies, National University of Singapore, Singapore 119007*

[5]*Frontier Science Center for Quantum Information, Beijing 100084, China*

[6]*Beijing National Research Center for Information Science and Technology, Beijing 100084, China*

(Received 16 August 2023; revised 7 May 2024; accepted 23 May 2024; published 12 June 2024)

There has been an increasing research focus on quantum algorithms for condensed matter systems recently, with a particular emphasis on calculating energy band structures. Here, we propose a quantum algorithm, the powered full quantum eigensolver (P-FQE), by using the power of operators of the full quantum eigensolver. This leads to an exponential increase in the success probability of measuring the target state in certain circumstances where the number of generating elements involved in the power of operators exhibits a log polynomial dependence on the number of orbitals. Furthermore, we conduct numerical calculations for the energy spectrum of the Fermi-Hubbard model and band-structure determination of the twisted double-layer graphene. We experimentally demonstrate the feasibility and robustness of the P-FQE algorithm using superconducting quantum computers for graphene and Weyl semimetal. One significant advantage of our algorithm is its ability to reduce the requirements of extremely high-performance hardware, making it more suitable for energy spectra determination on noisy intermediate-scale quantum devices.

DOI: 10.1103/PhysRevB.109.245117

I. INTRODUCTION

Feynman [1] pointed out that when classical computers were used to simulate quantum systems, resource consumption would exponentially increase. Nevertheless, by developing computing systems that work according to the laws of quantum mechanics, this difficulty can be avoided in principle. Quantum computation has gained considerable attention across various fields [2–10], harnessing its inherent quantum advantages. Quantum chemistry has emerged as one of the extensively studied applications, predominantly focused on atomic and molecular systems [11–15]. However, research efforts on more complex many-body systems such as solid-state systems are comparatively limited.

In solid-state physics, the concept of an energy band is fundamental, which describes the distribution of energy levels available to electrons as a function of the wave vector within the material [16,17]. Calculating energy band structures holds paramount significance in understanding the electronic properties of materials, designing novel materials, and interpreting material behaviors.

The prevailing quantum algorithms for calculating the electronic band structure use hybrid quantum-classical methods such as a variational quantum eigensolver (VQE) [18–21] for a ground state, and its modified versions for an excited state, such as variational quantum deflation (VQD) [22–24] and a subspace-search variational quantum eigensolver (SSVQE) [25,26]. These variational quantum algorithms (VQAs) are studied vigorously for their low-depth circuits [4,27]. They consist of parametrized quantum and classical optimizations. The classical optimizations optimize the expectation values measured from the quantum circuit to iterate parameters in the quantum circuit. The parametrized quantum circuit can be designed based on a problem-inspired ansatz or a hardware-efficient ansatz [4]. However, there are still some open questions concerning VQAs, such as the existence of barren plateaus [28] and the ambiguity surrounding a quantum advantage [29,30].

The full quantum eigensolver (FQE) algorithm was proposed for quantum chemistry simulations [31]. It simulates the objective Hamiltonian and performs gradient descent optimization entirely on a quantum computer. The parameters of quantum circuits in the FQE remain fixed throughout the iteration process and are determined by the objective Hamiltonian. With each iteration of the quantum gradient descent circuit, the state vector becomes progressively closer to the ground state. Moreover, the extended version of the FQE for an excited state, called a full quantum excited-state solver (FQESS), was proposed subsequently [32]. By utilizing the measurement results of the lower energy levels obtained from the quantum circuit, the Hamiltonian and the parameters in the circuit can be updated to target the next energy level. The ground state of the updated Hamiltonian corresponds to the eigenvector associated with the next energy level. However, the main drawback of these algorithms is that the success probability decreases significantly with each iteration, which

*weisj@baqis.ac.cn
†gllong@tsinghua.edu.cn

limits their applicability on noisy intermediate-scale quantum (NISQ) devices. To address this issue, we propose an algorithm here called the powered-FQE (P-QFE), which directly implements multiple powers of the operator instead of executing multiple iterations of the operator on the quantum computer. This approach can significantly reduce the actual number of real runs, and in extreme cases it can achieve convergence with just a single run.

This paper is organized as follows: In Sec. II, we present the framework of the P-FQE. We then apply the P-FQE to calculate the energy band structures of twisted double-layer graphene, and we compare the numerical simulation results with classical methods in Sec. III. In Sec. IV, we conduct experiments on two superconducting quantum computers (Quafu and IBM quantum cloud platform) to compare and validate the effectiveness and robustness of our algorithm. Finally, we provide a conclusion in Sec. V.

II. METHOD

A. The Hamiltonian of a condensed-matter system

In solid-state physics, a many-body system contains a collection of ion cores and a cloud of electrons interacting with each other. In the nonrelativistic case, the corresponding original Hamiltonian of the system can be expressed in first quantization as

$$H_{\text{or}} = -\sum_i \frac{\nabla_{R_i}^2}{2M_i} - \sum_i \frac{\nabla_{r_i}^2}{2} - \sum_{i,j} \frac{Z_i}{|R_i - r_j|} + \sum_{i,j>i} \frac{Z_i Z_j}{|R_i - R_j|} + \sum_{i,j>i} \frac{1}{|r_i - r_j|} \tag{1}$$

in atomic units ($\hbar = 1$). Here, R_i, Z_i, M_i, and r_i represent the positions, charges, masses of the ion cores, and the positions of the electrons, respectively. The computational resources needed to calculate the energy spectrum of a many-body system scale exponentially with the number of ion cores and electrons on a classical computer, making it intractable in high-dimension.

Under the Born-Oppenheimer approximation, which assumes the nuclei are stationary due to their much larger mass compared to electrons, we obtain the following second-quantized formulation of the Hamiltonian:

$$H = \sum_{ij} h_{ij} c_i^\dagger c_j + \frac{1}{2} \sum_{ijkl} h_{ijkl} c_i^\dagger c_j^\dagger c_k c_l + \cdots, \tag{2}$$

where $c_i^\dagger$ (c_i) are the creation (annihilation) operators on the site i. The parameters h_{ij} and h_{ijkl} are the one-particle and two-particle integrals for a specific basis function ϕ_i. We adopt the Jordan-Wigner (JW) transformation to map these fermionic operators to qubit operators by the following rules [33,34]:

$$\begin{aligned} c_i^\dagger &= \tfrac{1}{2} Z_1 \otimes Z_2 \otimes Z_{i-1} \otimes (X_i - iY_i) \otimes I_{i+1} \otimes \cdots, \\ c_i &= \tfrac{1}{2} Z_1 \otimes Z_2 \otimes Z_{i-1} \otimes (X_i + iY_i) \otimes I_{i+1} \otimes \cdots, \end{aligned} \tag{3}$$

where subscript i represents the single-particle state labeling. After transformations, the qubit Hamiltonian can be expressed as

$$H = \sum_i \alpha_i P_i, \tag{4}$$

where $P_i = \sigma_{i1} \otimes \sigma_{i2} \otimes \cdots$ is a tensor product of Pauli matrices, defined as a "Pauli word" with $\sigma \in \{I, X, Y, Z\}$. Since any Hamiltonian can be decomposed into Pauli terms, this method is universally applicable to a general system with interactions.

B. The quantum algorithm

1. Power iteration method

The power iteration method for computing eigenvalues and eigenvectors is valuable for estimating the eigenvectors of large and sparse matrices [35]. Assuming matrix A possesses n eigenstates u_i and the corresponding eigenvalues λ_i, the eigenfunctions can be expressed as $Au_i = \lambda_i u_i$. Due to the completeness of the eigenfunctions of the Hermitian operator, an arbitrary initial state of this quantum system can be fully described within the Hilbert space spanned by this set of eigenfunctions. This description involves representing the state as a linear superposition of eigenstates: $x^{(0)} = \sum_{i=0}^{n-1} a_i u_i$. Applying the tth power of A to $x^{(0)}$ yields

$$x^{(t)} = A^t x^{(0)} = \lambda_0^t \left[a_0 u_0 + \sum_{i=1}^{n-1} a_i \left(\frac{\lambda_i}{\lambda_0} \right)^t u_i \right]. \tag{5}$$

t in A^t is referred to as the "exponent" or "power." If the absolute values of the eigenvalues satisfy the inequality constraints $|\lambda_0| \geqslant |\lambda_1| \geqslant |\lambda_2| \cdots \geqslant |\lambda_n|$, then we have $\lim_{t\to\infty} (\lambda_i/\lambda_0)^t = 0$. So if the exponent t is sufficiently large, $x^{(t)}$ will approach the ground state u_0. This method can also be interpreted from the perspective of quantum gradient descent, as shown in Ref. [32], and we develop our quantum algorithm based on above process.

In FQE and FQESS algorithms, each iteration is essentially the evolution of quantum states under the same operator, but their probability of success decreases exponentially with the number of iterations. Our algorithm is based on the idea of reducing the number of iterations to improve the success probability, achieved by replacing the original evolution operator with the power of the operator itself. We analyze the power required and estimate the error in Appendix A. In our method, there exists a tradeoff between the number of required iterations and the power. For simplicity, we present our algorithm by employing a single run.

2. Estimation of the number of expansion terms

Realizing our algorithm on a quantum circuit requires the expansion of the evolution operator into a linear combination of unitary operators [36–42]. To reduce circuit complexity among other objectives, the specific form of the unitary expansion can be varied to suit the requirements of different problems, thereby simplifying the expansion form. Without a loss of generality, in this work the unitary expansion adopts the form of Pauli operators. The underlying premise for our algorithm's advantage is that the quantum circuit complexity related to the number of expansion terms does not increase at the same rate as the operator's exponent. Here we provide a

method for preliminary estimation of the number of expansion terms.

Since the coefficient $K = \{\pm 1, \pm i\}$ is not a concern, we will work with the following Abelian Pauli group [43]:

$$\tilde{\mathcal{P}}_n = \mathcal{P}_n / K = \{I, X, Z, XZ\}^{\otimes n}, \tag{6}$$

which is the quotient group over K and contains 4^n elements. Any operator A on an n-qubit system can be decomposed into a linear combination of Pauli operators:

$$A = \sum_{\sigma \in \tilde{\mathcal{P}}_n} \mu_\sigma \sigma. \tag{7}$$

Define S as the set of all terms with nonzero coefficient, $S = \{\sigma \in \tilde{\mathcal{P}}_n \mid \mu_\sigma \neq 0\}$, and let $G = \langle S \rangle$ be the subgroup of $\tilde{\mathcal{P}}_n$ generated by S. It then follows that any power of A can be decomposed into a linear combination of some subset of G.

To estimate the size of G, we utilize the isomorphic relation $\tilde{\mathcal{P}}_n \cong \mathbb{F}_2^{2n}$, where $\mathbb{F}_2^{2n}$ is a $2n$-dimensional linear space over a binary field $\mathbb{F}_2$. The isomorphism $\mathcal{M} : \tilde{\mathcal{P}}_n \leftrightarrow \mathbb{F}_2^{2n}$ can be constructed as follows:

$$\mathcal{M} : X_1^{x_1} \cdots X_n^{x_n} Z_1^{z_1} \cdots Z_n^{z_n} \mapsto (\mathbf{x}, \mathbf{z}), \tag{8}$$

where $\mathbf{x} = (x_1, \ldots, x_n) \in \mathbb{F}_2^n, \mathbf{z} = (z_1, \ldots, z_n) \in \mathbb{F}_2^n$. Then the multiplication in $\tilde{\mathcal{P}}_n$ corresponds to the addition in $\mathbb{F}_2^{2n}$, $\mathcal{M}(\sigma \cdot \omega) = \mathcal{M}(\sigma) + \mathcal{M}(\omega)$. Clearly, $\mathcal{M}$ maps G to a subspace spanned by the vector set $\mathcal{M}(S) = \{\mathcal{M}(\sigma)\}_{\sigma \in S}$. If there are l linearly independent vectors in $\mathcal{M}(S)$, then G is isomorphic to an l-dimensional subspace, implying the expansion of any power of A has at most $L = 2^l$ terms. To minimize algorithm complexity, it is desirable for l to be as small as possible. We refer to the aforementioned method as the vector encoding method.

For condensed-matter systems, due to the periodicity and lattice symmetry, their Hamiltonians are likely to exhibit a higher degree of symmetry. Therefore, it is reasonable to assume that the number of Pauli words in the Pauli expansion of the powers of their Hamiltonians increases slowly [44–46]. In Appendix B, we have selected six models and presented the relationship between the powers of their Hamiltonians and the number of terms in the Pauli expansion.

C. Quantum algorithm realization

For quantum chemistry and the band-structure problems, we generally start with a linear combination of Pauli words as shown in Eq. Eq. (4). When determining the band structure of a crystal, given a certain wave vector $\vec{k}$, we can express the Hamiltonian as $H_k = \sum_{i=0}^{M_k - 1} \alpha_i^{(k)} P_i$, where M_k is the number of Pauli words. The set of eigenvalues is denoted as $\{E_{j,k}\}_{j=1}^{2^n}$ with corresponding eigenstates $\{\varphi_{j,k}\}_{j=1}^{2^n}$. In general crystal systems, there are some bands with eigenvalues greater than zero. To ensure that all eigenvalues are less than zero, a bias term needs to be introduced, and the Hamiltonian is reconstructed as

$$U_{1,k} = H_k - \lambda_0 I^{\otimes n} (\lambda_0 > \max\{0, E_{1,k}, \ldots, E_{2^n,k}\}). \tag{9}$$

Typically, the larger the bias parameter λ_0, the more time-consuming the algorithm becomes. Therefore, it is desirable to minimize its value [32]. In general, the bias parameter λ_0 affects the one-norm of a reconstructed Hamiltonian and should be chosen properly, because it affects the ratio of reconstructed eigenvalues $(E_i - \lambda_0)/(E_1 - \lambda_0)$, which is related to the convergence rate of the algorithm. If λ_0 is significantly larger than E_i, the convergence speed will decrease. Some reduction technologies for the one-norm of a Hamiltonian can be adapted to improve the algorithm's performance [47,48].

The exponent required to obtain the ground state of $U_{1,k}$ is assumed to be $t_{1,k}$, and the operator $U_{1,k}$ raised to the power of $t_{1,k}$ can be expanded as

$$U_{1,k}^{t_{1,k}} = \sum_{i=0}^{L_{1,k}-1} \beta_i^{(1,k)} P_i, \tag{10}$$

where $L_{1,k} \leqslant 4^n$. The operator $U_{1,k}^{t_{1,k}}$ can be implemented in a quantum circuit. As Appendix B shows, in many practical physical systems, it is often observed that $L_{1,k}$ is significantly smaller than 4^n, and converges faster towards a relatively small value as $t_{1,k}$ increases. The coefficients $\beta_i^{(1,k)}$ for each Pauli word can be obtained through simple classical calculations, and we now shift our focus to the quantum circuit implementation of P-FQE.

The first step involves initializing the ancillary system and the work system. We take the computational basis $|i\rangle_s$ to represent the state of a quantum system. Here $|0\rangle_s$ denotes the initial state of ancillary system $|0\rangle^{\otimes l_{1,k}}$, where $l_{1,k} = \lceil \log_2 L_{1,k} \rceil$ is the number of ancillary qubits. The ancillary qubits are introduced to create a larger Hilbert space and are initialized from $|0\rangle_s$ to a specific state

$$|\psi_{1,k}\rangle = \frac{1}{\mathfrak{C}} \sum_{i=0}^{2^{l_{1,k}}-1} \beta_i^{(1,k)} |i\rangle_s, \tag{11}$$

where $\mathfrak{C} = \sqrt{\sum_{i=0}^{2^{l_{1,k}}-1} |\beta_1^{(1,k)}|^2}$ is the normalization constant.

When initializing the work system, using an appropriate basis set, such as a linear combination of atomic orbitals (LCAOs) or orthogonalized plane waves (OPWs), can significantly improve the efficiency of our algorithm [49,50]. Here we denote the trial initial state as $|\Phi_0^{(1,k)}\rangle$. In complex systems, the quantum random access memory (qRAM) method can be utilized to prepare the initial states [51].

The second step of the quantum circuit involves entangling the ancillary qubits with the work qubits using a series of controlled gate operations. If the ancillary qubits is in state $|i\rangle_s$, then the corresponding controlled gate acting on the work qubits would be Pauli word P_i. After entanglement, the entire system evolves into the state $(\sum_{i=0}^{L_{1,k}-1} \beta_i^{(1,k)} |i\rangle_s P_i |\Phi_0^{(1,k)}\rangle)/\mathfrak{C}$.

The final step involves performing a wave combination and measurement. By applying a Hadamard gate to each ancillary qubit, we execute the wave combination, and the entire space is transformed into

$$\frac{1}{\mathfrak{C}\sqrt{2^{l_{1,k}}}} \left(|0\rangle_s \otimes \sum_{i=0}^{L_{1,k}-1} \beta_i^{(1,k)} P_i |\Phi_0^{1,k}\rangle + \sum_{i=1}^{2^{l_{1,k}}} |i\rangle_s \otimes |\Psi_i\rangle \right), \tag{12}$$

where $|\Psi_i\rangle$ is the state of the work system in the subspace where the state of the ancillary system is $|i\rangle_s$. The work system

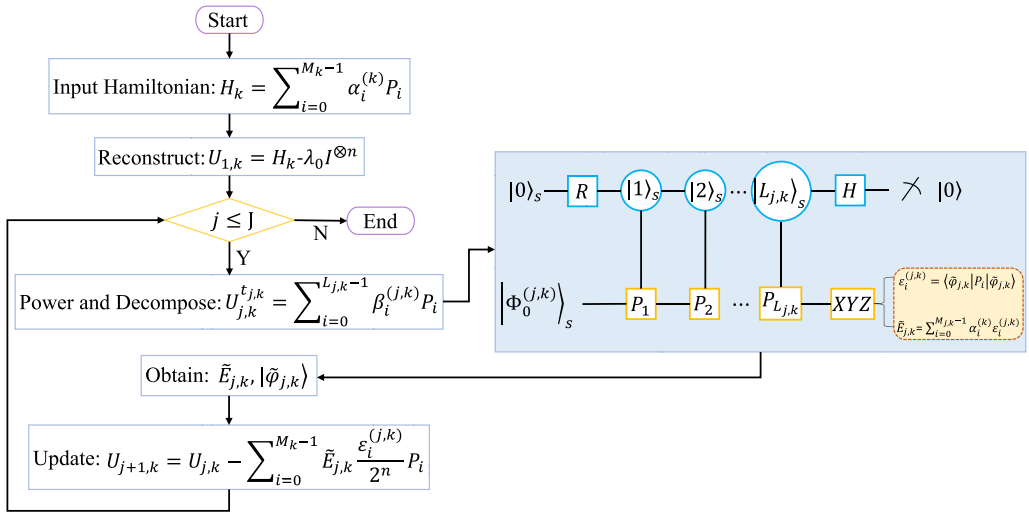

FIG. 1. The flow chart of P-FQE. Here J represents the highest energy band that needs to be determined, and it is generally adequate to focus solely on the properties of the systems within the low-energy regime when tackling electronic structure problems. The right panel illustrates the quantum circuit designed in our method, and XYZ represent Pauli measurements.

collapses to the approximate ground state $|\tilde{\varphi}_{1,k}\rangle$ of H_k when the ancillary system is measured as $|0\rangle_s$.

The probability of successfully obtaining the target state is $P_s = \|U_{1,k}^{t_{1,k}}|\Phi_0^{(1,k)}\rangle\|/(\mathbb{C}^2 2^{l_{1,k}})$. While in the FQE algorithm, the probability of success is $P_{s(\mathrm{FQE})} = [\|U_{1,k}|\Phi_0^{(1,k)}\rangle\|/(\mathbb{C}^2 2^{m_k})]^{t_{1,k}}$, and it declines exponentially with the number of iteration steps $t_{1,k}$ with $\mathbb{C} = \sqrt{\sum_{i=0}^{M_k-1} \alpha_i^2}$ [31,52], where $m_k = \lceil \log_2 M_k \rceil$. And the noise in each iteration will further affect the probability of success. As long as $L_{1,k}$ does not exhibit exponential growth with respect to M_k, we can conclude that our algorithm exponentially increases the probability of success compared to FQE, or equivalently, it exponentially reduces the measurement complexity.

We use Pauli measurements to estimate the approximate eigenvalue $\tilde{E}_{1,k}$ corresponding to $|\tilde{\varphi}_{1,k}\rangle$,

$$\varepsilon_i^{(1,k)} = \langle\tilde{\varphi}_{1,k}|P_i|\tilde{\varphi}_{1,k}\rangle, \tag{13}$$

$$\tilde{E}_{1,k} = \langle\tilde{\varphi}_{1,k}|H_k|\tilde{\varphi}_{1,k}\rangle = \sum_{i=0}^{M_{1,k}-1} \alpha_i^{(k)} \varepsilon_i^{(1,k)}, \tag{14}$$

where $\varepsilon_i^{(1,k)}$ can be obtained by repeated measurements of Pauli word P_i. To obtain the higher excited state and excited energy of H_k, we use a procedure similar to FQESS and VQD [22–24,32]. We update the original operator as

$$\begin{aligned} U_{2,k} &= H_k - \tilde{E}_{1,k}|\tilde{\varphi}_{1,k}\rangle\langle\tilde{\varphi}_{1,k}| - \lambda_0 I^{\otimes n} \\ &= \sum_{i=0}^{M_k-1} \left(\alpha_i^{(k)} - \tilde{E}_{1,k} \frac{\varepsilon_i^{(1,k)}}{2^n}\right) P_i - \lambda_0 I^{\otimes n}, \end{aligned} \tag{15}$$

whose ground state corresponds to the first excited state of H_k. The new operator implemented in the quantum circuit is $U_{2,k}^{t_{2,k}} = \sum_{i=0}^{L_{2,k}-1} \beta_i^{(2,k)} P_i$. The subsequent steps follow the same procedure as described above. To obtain the energy spectrum corresponding to a specific k-point, it is necessary to initialize the work qubits in a state that has a nonzero overlap with the target eigenstate for a specific energy level. For example, we can use the superposition state of the computational basis states $\sum_{i=0}^{n} \frac{1}{\sqrt{n}}|i\rangle$ as the initial state of the work qubits to find any energy level.

By iterating the aforementioned procedure, the entire energy spectrum for the Hamiltonian H_k can be obtained. By systematically varying the values of k along high-symmetry paths and obtaining the corresponding Hamiltonians, we can repeatedly perform the previously described procedure to determine the complete energy band structure of the target crystal. The detailed steps of the P-FQE algorithm are illustrated in the algorithm flowchart shown in Fig. 1.

D. Complexity analysis

The complexity of the P-FQE algorithm consists of classical and quantum computation components. We take the calculation of the energy spectrum H_k as an example. The Pauli expansion of the operator, calculated on a classical computer, involves multiplying the weight coefficients of each Pauli word, with the coefficients below a certain threshold being discarded during the process. The complexity of the classical part is $O(M_k^{\log_2 t_k})$, where M_k is the number of expansion terms of the original Hamiltonian, $t_k = \max\{t_{j,k}\}$. Moreover, we introduce another circuit updating method in Appendix C, which can further reduce the complexity of constructing a quantum circuit for computing excited states.

For the complexity of the quantum computing part, we consider gate complexity and measurement complexity. According to Sec. II B 2, if there are l_k linearly independent vectors in $\mathcal{M}(S_k)$, where $S_k = \{P_i \in \tilde{\mathcal{P}}_n \mid \alpha_i^{(k)} \neq 0\}$, let $\max\{L_{j,k}\} = L_k$, then $L_k \leqslant 2^{l_k}$. The maximum total number of basic gates needed to obtain the energy spectrum is $O(JL_k \log_2 L_k)$ [32,53–55], where J represents the highest energy band that needs to be determined. The number of work qubits required by P-FQE is $\lceil \log_2 D(H_k) \rceil$, the same as in the FQE algorithm, where $D(H_k)$ represents the matrix dimension of H_k. The maximum number of ancillary qubits required by P-FQE is $\lceil \log_2 L_k \rceil$, while FQE requires

$\lceil \log_2 M_k \rceil$. Due to the logarithmic relationship between the number of ancillary qubits and the number of expansion terms, the additional qubits required by P-FQE are relatively few. Our method achieves an exponential reduction in measurement complexity compared to the FQE method, on the condition that L_k does not exhibit exponential growth with respect to M_k. This condition is typically satisfied, as L_k is subject to an upper limit constraint, and empirical results are often better, as evidenced in Appendix B. In general, the number of orbitals is polynomially related to the number of terms in the Hamiltonian. Therefore, our method achieves an exponential increase in the success probability of measuring the target state when l_k exhibits a log polynomial dependence on the number of orbitals. The measurement complexity is $O(\sqrt{L_k})$ when the technique of quantum amplitude amplification is employed to further enhance the success probability [56,57].

III. NUMERICAL SIMULATION FOR THE FERMI-HUBBARD MODEL AND ELECTRONIC BAND STRUCTURE

A. Fermi-Hubbard model

In this section, we use our method to determine the energy spectrum of the Fermi-Hubbard model. The Hamiltonian of the Fermi-Hubbard model in real space can be described as

$$\hat{H}_{\mathrm{FH}} = -J \sum_{\langle ij\rangle,\sigma} \hat{c}^{\dagger}_{i\sigma}\hat{c}_{j\sigma} + U \sum_{i} \left(\hat{n}_{i\uparrow} - \frac{1}{2}\right)\left(\hat{n}_{i\downarrow} - \frac{1}{2}\right) - \mu \sum_{i} (\hat{n}_{i\uparrow} + \hat{n}_{i\downarrow}) - h \sum_{i} (\hat{n}_{i\uparrow} - \hat{n}_{i\downarrow}), \tag{16}$$

where $\hat{c}^{\dagger}_{i\sigma}(\hat{c}_{i\sigma})$ are creation (annihilation) operators acting at the ith site with spin σ, $n_{i\sigma} = \hat{c}^{\dagger}_{i\sigma}\hat{c}_{i\sigma}$ is the number operator, and $\langle i, j\rangle$ denotes adjacent sites on a square lattice. μ represents the chemical potential, and h represents the external magnetic field.

Considering a dimer lattice that accommodates one spin-up electron and one spin-down electron, the Hamiltonian simplifies to

$$\hat{H}_{\mathrm{FH}} = -J(\hat{c}^{\dagger}_{1\uparrow}\hat{c}_{2\uparrow} + \hat{c}^{\dagger}_{2\uparrow}\hat{c}_{1\uparrow} + \hat{c}^{\dagger}_{1\downarrow}\hat{c}_{2\downarrow} + \hat{c}^{\dagger}_{2\downarrow}\hat{c}_{1\downarrow}) + U\left(\hat{n}_{1\uparrow} - \tfrac{1}{2}\right)\left(\hat{n}_{1\downarrow} - \tfrac{1}{2}\right) + U\left(\hat{n}_{2\uparrow} - \tfrac{1}{2}\right)\left(\hat{n}_{2\downarrow} - \tfrac{1}{2}\right). \tag{17}$$

As $n_\uparrow + n_\downarrow$ is a conserved quantity, the simplified Hamiltonian is

$$\hat{H}_{\mathrm{FH}} = -J(\hat{c}^{\dagger}_{1\uparrow}\hat{c}_{2\uparrow} + \hat{c}^{\dagger}_{2\uparrow}\hat{c}_{1\uparrow} + \hat{c}^{\dagger}_{1\downarrow}\hat{c}_{2\downarrow} + \hat{c}^{\dagger}_{2\downarrow}\hat{c}_{1\downarrow}) + U\hat{n}_{1\uparrow}\hat{n}_{1\downarrow} + U\hat{n}_{2\uparrow}\hat{n}_{2\downarrow}. \tag{18}$$

For $\hat{d}_1 = \hat{c}_{1\uparrow}$, $\hat{d}_2 = \hat{c}_{2\uparrow}$, $\hat{d}_3 = \hat{c}_{1\downarrow}$, $\hat{d}_4 = \hat{c}_{2\downarrow}$, we have

$$\hat{H}_{\mathrm{FH}} = -J(\hat{d}^{\dagger}_1\hat{d}_2 + \hat{d}^{\dagger}_2\hat{d}_1 + \hat{d}^{\dagger}_3\hat{d}_4 + \hat{d}^{\dagger}_4\hat{d}_3) - U(\hat{d}^{\dagger}_3\hat{d}^{\dagger}_1\hat{d}_3\hat{d}_1 + \hat{d}^{\dagger}_4\hat{d}^{\dagger}_2\hat{d}_4\hat{d}_2). \tag{19}$$

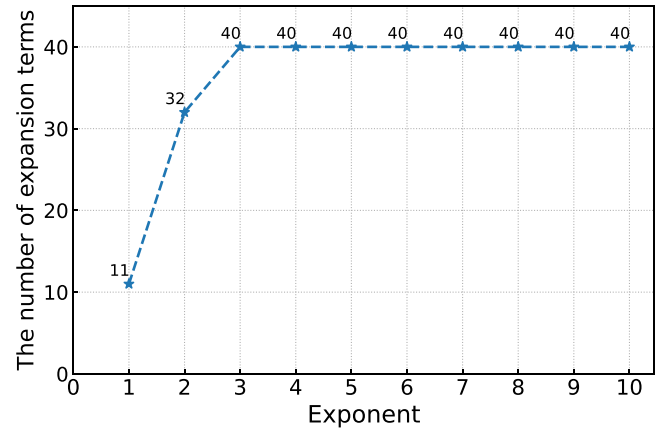

(a)

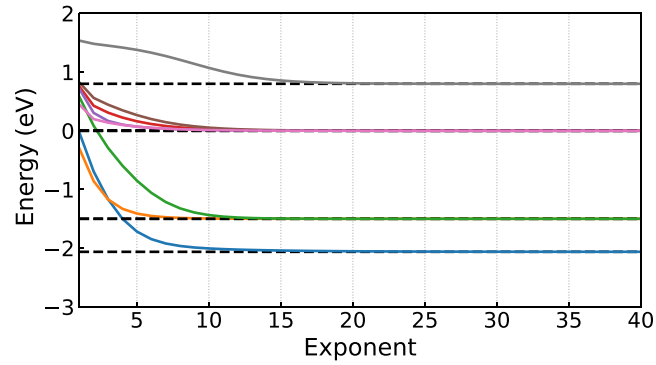

(b)

FIG. 2. (a) The relationship between the number of terms in the Pauli expansion and the exponent of the power of the Hamiltonian. (b) The numerical simulation results of the spectrum using the P-FQE algorithm. We present the results for the first four energy levels without considering degeneracy. The exact values obtained by Hamiltonian diagonalization are plotted by dashed lines. The numerical results plotted by solid lines converge to exact values as the operators are raised to a higher power.

Letting $J = 1.5$, $U = 2.3$, after the JW transformation, we have

$$\hat{H}_{\mathrm{FH}} = 1.15I - 0.75X_1X_2 - 0.75Y_1Y_2 - 0.575Z_1 + 0.575Z_1Z_3 - 0.575Z_2 + 0.575Z_2Z_4 - 0.75X_3X_4 - 0.75Y_3Y_4 - 0.575Z_3 - 0.575Z_4. \tag{20}$$

From Fig. 2, it is evident that the number of terms in the Pauli expansion of the power of the Hamiltonian of the Fermi-Hubbard model rapidly converges to a smaller value as the exponent increases. The numerical simulation results of the P-FQE algorithm also converge to the exact spectrum after raising the operators to a specific power.

B. Energy band calculation

For energy band calculations, we use a tight-binding (TB) Hamiltonian as an example to demonstrate the efficiency of our algorithms. In the TB approximation, only hopping terms among nearest-neighbor sites need to be considered

[58,59]. The total energy, comprising both the interaction energy and the kinetic energy, can be consolidated into the hopping term, while the potential energy term or on-site energy simply adds a constant. In the second quantization formalism, the TB Hamiltonian of a crystal can be expressed as $H = \sum_{\langle i,j\rangle,m,n} t_{ij,mn} c^{\dagger}_{i,m} c_{j,n}$, where m and n represent atomic orbitals, $\langle i, j\rangle$ denote pairs of nearest-neighbor lattice sites, $c^{\dagger}_{i,m}$ ($c_{i,m}$) are the creation (annihilation) operators acting at the orbital m and the site i, $t_{ij,mn}$ represents the hopping parameter between corresponding orbitals and sites, and it can be calculated as $t_{ij,mn} = \langle R_{mi}|h(\vec{r})|R_{nj}\rangle$, where $\{R_{mi}\}$ are the Wannier functions. In the TB approximation, the Wannier functions can be replaced with atomic orbital functions. Performing a Fourier transform of the creation and annihilation operators in the Wannier representation yields the TB Hamiltonian (H_k) in the Bloch representation.

We use twisted double-layer graphene as the demonstration model to numerically validate our algorithm. In double-layer graphene, interlayer interactions modify the electronic band structure, resulting in tunable electronic properties. Different stacking structures can be achieved by adjusting the twist angle between the layers. This composite structure gives rise to a set of long-period patterns known as moiré patterns on the underlying atomic lattice for certain twist angles [13,60,61]. Bistritzer and MacDonald [60] constructed a low-energy continuum effective Hamiltonian for twisted double-layer graphene, applicable to arbitrary translation vectors and twist angles $\theta \lesssim 10^{\circ}$, regardless of whether the structure is commensurate. The Hamiltonian expanded around the K-point of the Bistritzer-MacDonald model is

$$H_K(\mathbf{r}) = \begin{pmatrix} -i v_F \sigma \cdot \nabla & T(\mathbf{r}) \\ T^{\dagger}(\mathbf{r}) & -i v_F \sigma \cdot \nabla \end{pmatrix}, \tag{21}$$

/vskip4ptwhere $T(\mathbf{r})$ is the interlayer hopping term, and v_F is the Fermi velocity. We set the parameters to be the same as those in Ref. [60] with lattice constant $a_0 = \sqrt{3}\times 1.42$ Å and interlayer hopping energy $w = 110$ meV. The plane-wave expansion method is employed to numerically solve for the electronic spectrum, truncating the momentum-space lattice at the third honeycomb shell. The size of the Hamiltonian matrix is 196×196. Expanding the Hamiltonian for twisted bilayer graphene with a twist angle of 1.05° and $k_x = k_y = 0$ in the basis of Pauli words generates a total of 5440 terms. The Pauli expansion terms with coefficients exceeding 0.1, rounded to three decimal places, are listed below, with all "⊗" symbols omitted,

$$\begin{aligned} H =& 4.622 I_0I_1I_2I_3I_4I_5I_6Y_7 + 1.413 I_0Z_1I_2I_3I_4I_5I_6Y_7 \\ &+ 1.223 Z_0I_1I_2I_3I_4I_5I_6Y_7 - 0.356 I_0Z_1Z_2I_3I_4I_5I_6Y_7 \\ &- 0.234 I_0Z_1I_2I_3Z_4I_5I_6Y_7 - 0.199 Z_0I_1Z_2I_3Z_4Z_5I_6Y_7 \\ &+ 0.198 Z_0Z_1Z_2I_3Z_4I_5I_6Y_7 - 0.191 I_0Z_1Z_2I_3I_4I_5I_6X_7 \\ &- 0.171 I_0Z_1Z_2Z_3Z_4Z_5I_6Y_7 + 0.170 Z_0Z_1I_2I_3Z_4Z_5I_6Y_7 \\ &+ 0.164 Z_0Z_1Z_2Z_3I_4Z_5I_6Y_7 - 0.164 Z_0I_1Z_2Z_3Z_4I_5I_6Y_7 \\ &+ 0.164 I_0I_1I_2I_3Z_4Z_5I_6Y_7 - 0.137 Z_0I_1I_2Z_3I_4I_5I_6Y_7 \\ &- 0.137 Z_0I_1I_2Z_3Z_4Z_5I_6Y_7 + 0.137 I_0I_1Z_2I_3Z_4Z_5I_6Y_7 \\ &- 0.136 I_0Z_1Z_2I_3I_4Z_5I_6Y_7 + 0.136 Z_0Z_1I_2Z_3Z_4I_5I_6Y_7 \\ &+ 0.136 Z_0Z_1I_2Z_3I_4I_5I_6Y_7 + 0.136 I_0I_1Z_2I_3Z_4I_5I_6Y_7 \\ &- 0.130 Z_0I_1Z_2I_3Z_4I_5I_6Y_7 + 0.129 Z_0Z_1Z_2I_3I_4Z_5I_6Y_7 \\ &+ 0.129 I_0I_1I_2Z_3I_4Z_5I_6Y_7 - 0.129 I_0Z_1I_2Z_3I_4Z_5I_6Y_7 \\ &+ 0.129 I_0I_1I_2Z_3Z_4Z_5I_6Y_7 + 0.129 I_0I_1I_2Z_3Z_4I_5I_6Y_7 \\ &- 0.129 I_0Z_1I_2Z_3I_4I_5I_6Y_7 - 0.129 Z_0I_1Z_2I_3I_4Z_5I_6Y_7 \\ &+ 0.128 Z_0Z_1Z_2I_3Z_4Z_5I_6Y_7 - 0.128 Z_0I_1I_2I_3I_4I_5I_6X_7 \\ &+ 0.110 I_0I_1Z_2Z_3I_4Z_5Z_6Y_7 - 0.108 Z_0Z_1I_2I_3I_4I_5I_6X_7 \\ &- 0.102 Z_0I_1I_2I_3Z_4Z_5I_6Y_7 - 0.102 I_0Z_1Z_2Z_3I_4Z_5I_6Y_7 \\ &+ 0.102 I_0I_1Z_2Z_3Z_4I_5I_6Y_7 + 0.102 I_0I_1Z_2Z_3Z_4Z_5I_6Y_7 \\ &- 0.101 Z_0I_1I_2I_3I_4Z_5I_6Y_7 + 0.101 Z_0Z_1I_2I_3Z_4I_5I_6Y_7 \\ &+ 0.101 I_0I_1Z_2Z_3I_4I_5I_6Y_7 - 0.101 I_0Z_1Z_2Z_3I_4I_5I_6Y_7 \\ &+ 0.101 Z_0Z_1I_2I_3I_4Z_5I_6Y_7 + 0.101 I_0I_1Z_2Z_3I_4Z_5I_6Y_7 \cdots . \end{aligned} \tag{22}$$

The moiré band structures for three twist angles $\theta = 5^{\circ}$, 1.05°, and 0.5° obtained through numerical simulation of P-FQE and the matrix diagonalization method are shown in Fig. 3. For twist angles of 5°, 1.05°, and 0.5°, the bias term λ_0 was set to 9.8, 2.3, and 1.2, respectively. We select a set of randomly orthogonal basis states as the initial states for the work qubits at each k-vector when computing different energy bands. For convenience, we directly use the 400th power of the initial Hamiltonian as the operator acting on the initial state in the quantum circuit for $\theta = 0.5^{\circ}$ and 1.05°, and the final counts of Pauli expansion terms are 62 694 and 63 939, respectively. For $\theta = 5^{\circ}$, we directly use the 230th power of its initial Hamiltonian, yielding 63 730 Pauli terms after expansion. The number of work qubits required for the three models is $\lceil \log_2 196 \rceil = 8$ each. Furthermore, the quantum circuit for the model of $\theta = 0.5^{\circ}$ requires $\lceil \log_2 62\,694 \rceil = 16$ ancillary qubits, and similarly, the other two also require 16 ancillary qubits. Thus, each of these three models requires a total of 24 qubits. More details are elaborated on in Appendix D.

The moiré bands in the first row represent the theoretical results obtained through classical diagonalization, which are consistent with those presented in the paper by Bistritzer and MacDonald [60]. The moiré bands in the second row are the numerical simulations obtained using our algorithm, which show good agreement with the theoretical expectations. As the twist angle decreases, the number of bands within a specific energy range increases and the band separation decreases, leading to a higher density of states. When $\theta = 1.05^{\circ}$, the Dirac-point velocity vanishes, resulting in a very flat band that implies strong correlation effects. It is worth mentioning that the spectrum results at points with smaller energy gaps are more sensitive to the value of the exponent, leading to less smooth results compared to other points under the same parameter setup. This can be improved by increasing the exponent or introducing suitable bias value. For our numerical simulations with the P-FQE algorithm, we used matrix multiplication with Python rather than a quantum computer simulator.

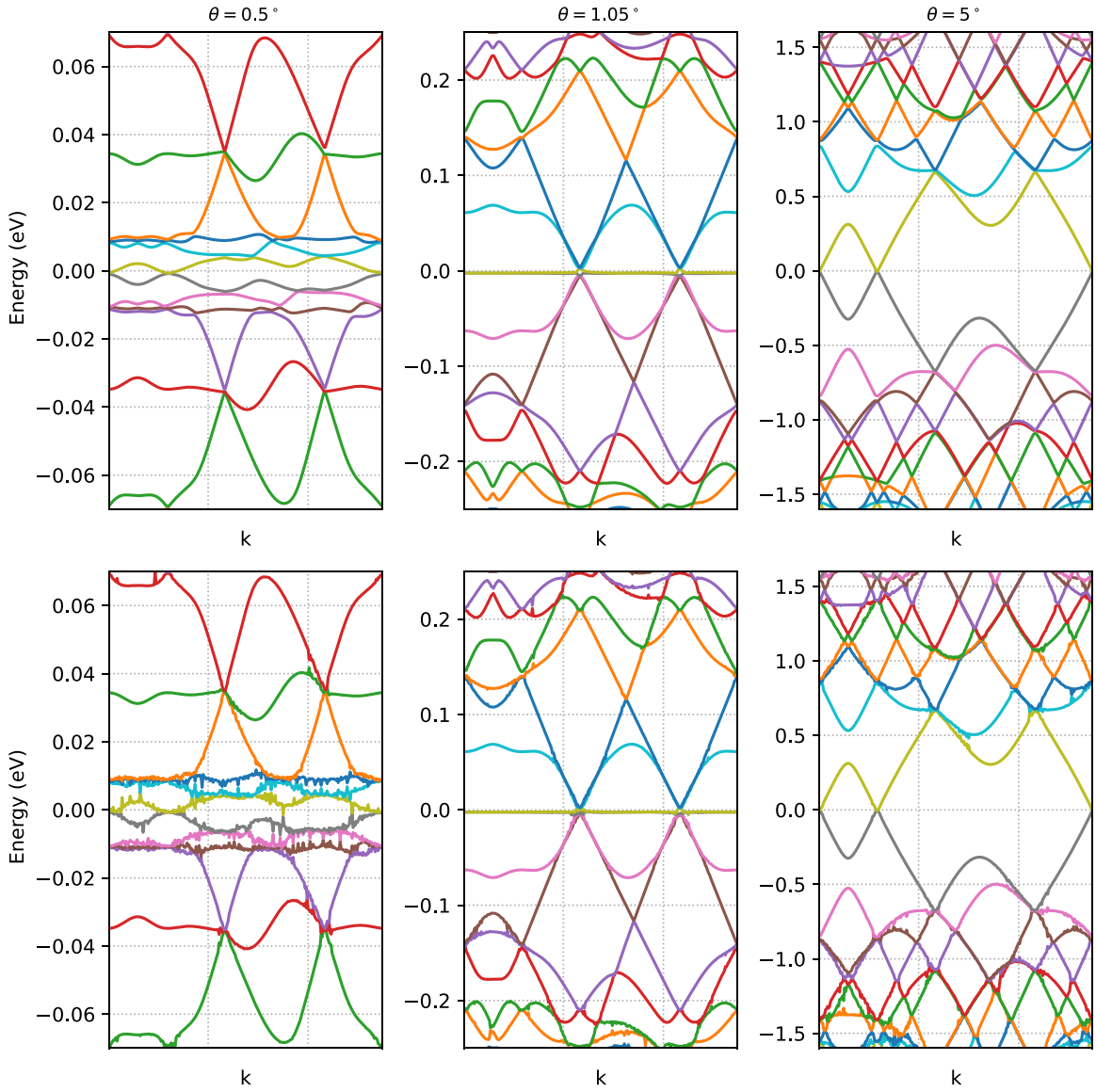

FIG. 3. The comparison of moiré bands in twisted double-layer graphene obtained from classical diagonalization (the first row) and numerical simulations of our P-FQE algorithm (the second row). Here $w = 110$ meV, and twist angles $\theta = 0.5^\circ$ (the first column), 1.05° (the second column), and 5° (the third column).

IV. RESULTS ON REAL QUANTUM DEVICES

In this section, we present two experimental demonstrations of the P-FQE algorithm with different physical systems (Weyl semimetal and graphene) on the superconducting quantum computing chips from Quafu/IBM quantum cloud platforms. Details of the two chips can be found in Appendix E, and we introduce the experimental process and results below.

A. Weyl semimetal

The first model we chose is the Weyl semimetal, a special topological material with a nontrivial band structure. In Weyl semimetals, the valence band and conduction band intersect at specific momentum space positions, forming Weyl points [62–65]. The energy bands near these points exhibit Dirac-like linear dispersion with relativistic features, forming a cone-shaped Fermi surface known as the Weyl cone. Weyl semimetals are of significant research interest in the field of topological physics and hold great potential for applications in novel electronic devices, optical materials, and topological quantum computation. The Hamiltonian for the minimal model of a Weyl semimetal is [66]

$$H = A(k_x * \sigma_x + k_y * \sigma_y) + \left[M_0 - M_1\left(k_x^2 + k_y^2 + k_z^2\right)\right]\sigma_z, \tag{23}$$

where parameters are set as $M_0 = M_1 = A = 1$, $k_x = k_y = 0$. So the Hamiltonian can be reduced to $H_{kz} = (1 - k_z^2)\sigma_z$, and the energy spectrum is a function of k_z. We set the bias parameter $\lambda_0 = 4$, and the value of power $t_{j,k} = 20$. Then the operator implemented on the quantum circuit is $(H_{k_z} - 4I)^{20}$ for the ground energy band. After obtaining the ground energy

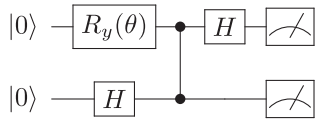

FIG. 4. The quantum circuit used to obtain the energy bands of the minimal model of a Weyl semimetal. This circuit requires only one ancillary qubit and one work qubit, entangled via a controlled-Z gate. The rotation angle θ in the $R_y(\theta)$ gate is modified as a function of energy levels and wave vector k_z in the simulation.

E_{1,k_z} and corresponding ground state $|\varphi_{1,k_z}\rangle$ for H_{k_z}, we implemented $(H_{k_z} - E_{1,k_z}|\varphi_{1,k_z}\rangle\langle\varphi_{1,k_z}| - 4I)^{20}$ on the circuit for obtaining the excited energy band. This is a simple model that can be executed with high fidelity on quantum devices, with one qubit as an ancillary qubit and another one as a work qubit. Due to the peculiar nature of the eigenstates of the model, a Hadamard gate is applied to the work qubit to initialize it in a superposition state of $|0\rangle$ and $|1\rangle$. The quantum circuit is shown in Fig. 4.

Figure 5 presents the band spectrum of a Weyl semimetal obtained from the classical calculation (solid lines), numerical simulation of P-FQE (dashed line), and experimental results of the P-FQE algorithm (error bar). The experiments are conducted on the Quafu quantum cloud platform [67]. Seven values of $k_z \in -2, -1.4, -0.6, 0, 0.7, 1.3, 2$ were used in the experiment. For different k_z values and energy bands, the Hamiltonian changes, and the ancillary qubit rotates by a different angle around the Y-axis, while the quantum circuit remains unchanged. For each k-vector, we performed three experimental trials, taking 40 000 samples per trial. The error bars are plotted using the average, minimum, and maximum values of the three trials. The experimental results of the P-FQE algorithm show good agreement with the theoretical values and numerical simulations. Two energy bands intersect at symmetric points, forming a pair of Weyl points. Due to the

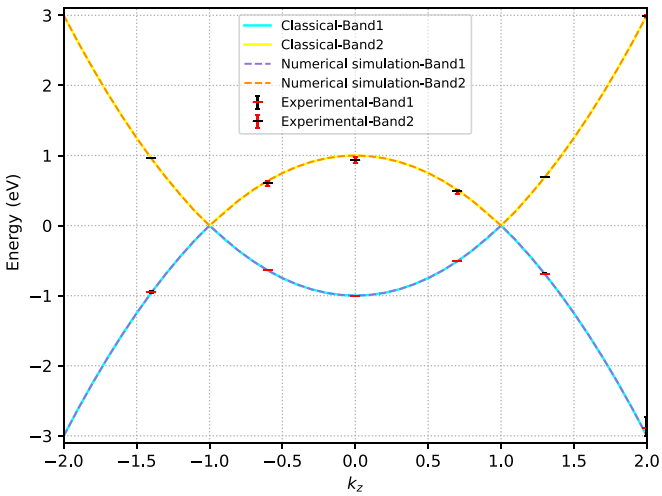

FIG. 5. Experimental results of the energy band structure for a Weyl semimetal as a function of k_z. Solid lines denote the classical computation results, while dashed lines indicate the classical simulation results of the P-FQE algorithm. Error bars show the experimental results from the superconducting quantum computing platform.

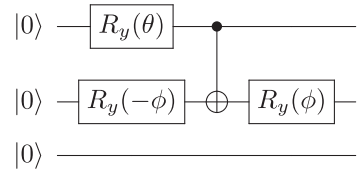

FIG. 6. The initialization part of the quantum circuits for calculating the band structure of single-layer graphene. The ancillary qubits are initialized to the state of $\cos\frac{\theta}{2}|0\rangle|0\rangle - \sin\phi\sin\frac{\theta}{2}|1\rangle|0\rangle + \cos\phi\sin\frac{\theta}{2}|1\rangle|1\rangle$.

simplicity of the model, the eigenstates can often be measured accurately in experiments, resulting in very small or even zero error bars.

B. Graphene

The second model for the experiments is single-layer graphene [68–71], a two-dimensional crystal with a hexagonal honeycomb lattice structure composed of carbon atoms exhibiting SP2 hybridization. This distinctive lattice arrangement causes the conduction and valence bands of graphene to intersect at the K point in the Brillouin zone, resulting in its zero-band-gap semiconductor characteristics. The Hamiltonian can be expressed as

$$H_k = \left(2\cos\frac{k_y}{2\sqrt{3}}\cos\frac{k_x}{2} + \cos\frac{k_y}{\sqrt{3}}\right)\sigma_x + \left(2\sin\frac{k_y}{2\sqrt{3}}\cos\frac{k_x}{2} - \sin\frac{k_2}{\sqrt{3}}\right)\sigma_y. \quad (24)$$

After introducing a bias term $-4I$, the Hamiltonian contains three terms (I, σ_x, and σ_y). For any power n, we have $(A\sigma_x + B\sigma_y - 4I)^n = a\sigma_x + b\sigma_y + cI$, which does not change the number of expansion terms. Therefore, we only need two ancillary qubits ($\lceil\log_2 3\rceil$) and a single work qubit. Here we consider the 25th power of the Hamiltonian.

The quantum circuit is divided into three parts. The first part initializes the ancillary register from $|0\rangle|0\rangle$ to the superposition state $\cos\frac{\theta}{2}|0\rangle|0\rangle - \sin\phi\sin\frac{\theta}{2}|1\rangle|0\rangle + \cos\phi\sin\frac{\theta}{2}|1\rangle|1\rangle$, corresponding to the terms I, σ_x, and σ_y, respectively, as shown in Fig. 6. The second part involves controlled operations on the work qubit (COX and CCY). Since $\sigma_y = i\sigma_x\sigma_z$, the circuit can be simplified as shown in Fig. 7. The $C^2(Z)$ gate can be further decomposed into a series of controlled-U gates. The third part is the measurement. We only need to measure σ_x and σ_y results by applying the Hadamard gate and $R_x(\pi/2)$ gates before measuring in the computational basis. To calculate the second energy band, the

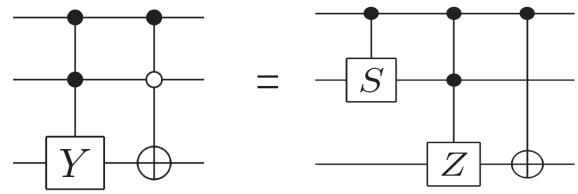

FIG. 7. The left $C^2(Y)-$COX gate is equivalent to the right circuit.

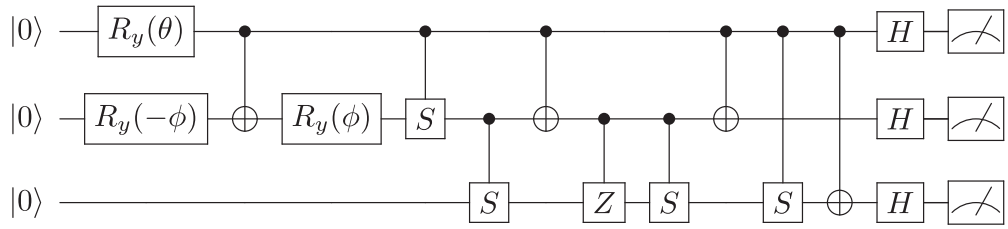

FIG. 8. Quantum circuit for computing the band structure of single-layer graphene on the superconducting quantum computer ibm_nairobi. The figure displays the circuit diagram for computing the first energy band and measuring the Pauli X. When computing the second energy band, add an X gate to initialize the work qubit to the state $|1\rangle$. When measuring the Pauli Y, replace the Hadamard gate acting on the work qubit before measurement with a rotation gate $R_x(\pi/2)$.

work qubit is initialized to $|1\rangle$ by applying an X gate. The final quantum circuit we run on the IBM cloud platform is shown in Fig. 8, which is applied for the first band and measured Pauli-X.

Due to the relatively high complexity of the second experimental model, requiring a deeper quantum circuit and a larger number of control gates, it imposes higher hardware requirements. Therefore, we choose the IBM quantum chip ibm_nairobi as the platform for our second experiment. We selected seven experimental points along the high-symmetry path ($K \to \Gamma \to M \to K$) in the reciprocal space of graphene. In addition to the selected k-points Λ : $(\frac{\sqrt{3}\pi}{9a}, \frac{\pi}{3a})$, $\Gamma : (0,0)$, $\Sigma : (0, \frac{\pi}{3a})$, and $M : (0, \frac{2\pi}{3a})$, we have also chosen one k-point along each of the paths from Γ to Σ, Σ to M, and M to K. These additional k-points are $(0, \frac{3\pi}{18a})$, $(0, \frac{\pi}{2a})$, and $(\frac{\sqrt{3}\pi}{9a}, \frac{2\pi}{3a})$. For the first two k-points, the absence of the Pauli Y term in their Hamiltonian allows us to perform the experiments using only two qubits in practice. For each k-point, we conducted three trials and plotted error bars, with each experiment consisting of 40 000 samples. As shown in Fig. 9, the numerical simulation results of the P-FQE algorithm align perfectly with the theoretical values. However, there may be slight discrepancies in the experimental results, but the overall trend remains consistent. The experimental data for both experiments are presented in Appendix F.

V. CONCLUSIONS

In summary, the P-FQE algorithm addressed the issue of exponential decay of the success probability with increasing iterations in FQE by substituting the original operator with its powers. Meanwhile, the P-FQE does not require a lot of additional ancillary qubits. We use this algorithm to study band-structure and energy spectrum calculations, and it suits many kinds of Hamiltonian problems. Additionally, we proposed the vector encoding method to estimate the maximum number of expansion terms of the power of operators, which can also be used to determine the truncation order in a Taylor series as discussed in Ref. [57]. The P-FQE algorithm is more suitable for current quantum computers because of reducing the real runs. We conducted numerical simulations on the Fermi-Hubbard model and double-layer graphene model, alongside two experiments on different

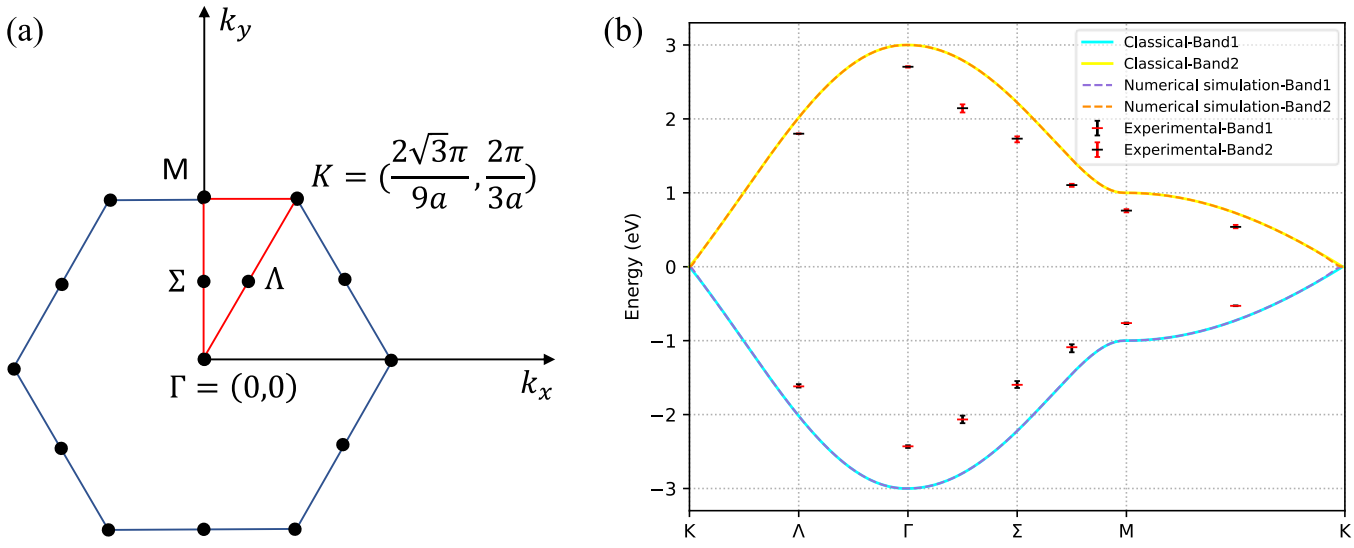

FIG. 9. The energy band structure of single-layer graphene. (a) The Brillouin zone of single-layer graphene with the high-symmetry k-points with $\Lambda = (\frac{\sqrt{3}\pi}{9a}, \frac{\pi}{3a})$, $\Gamma = (0,0)$, $\Sigma = (0, \frac{\pi}{3a})$, $M = (0, \frac{2\pi}{3a})$. (b) The energy bands depicted along the axis of high symmetry ($K \to \Gamma \to M \to K$) in the momentum space of graphene. The solid lines represent the energy bands obtained from classical computations, while the dashed lines depict the results obtained through numerical simulation of the P-FQE algorithm. The error bars illustrate the experimental measurements of the P-FQE algorithm conducted on ibm_nairobi chips.

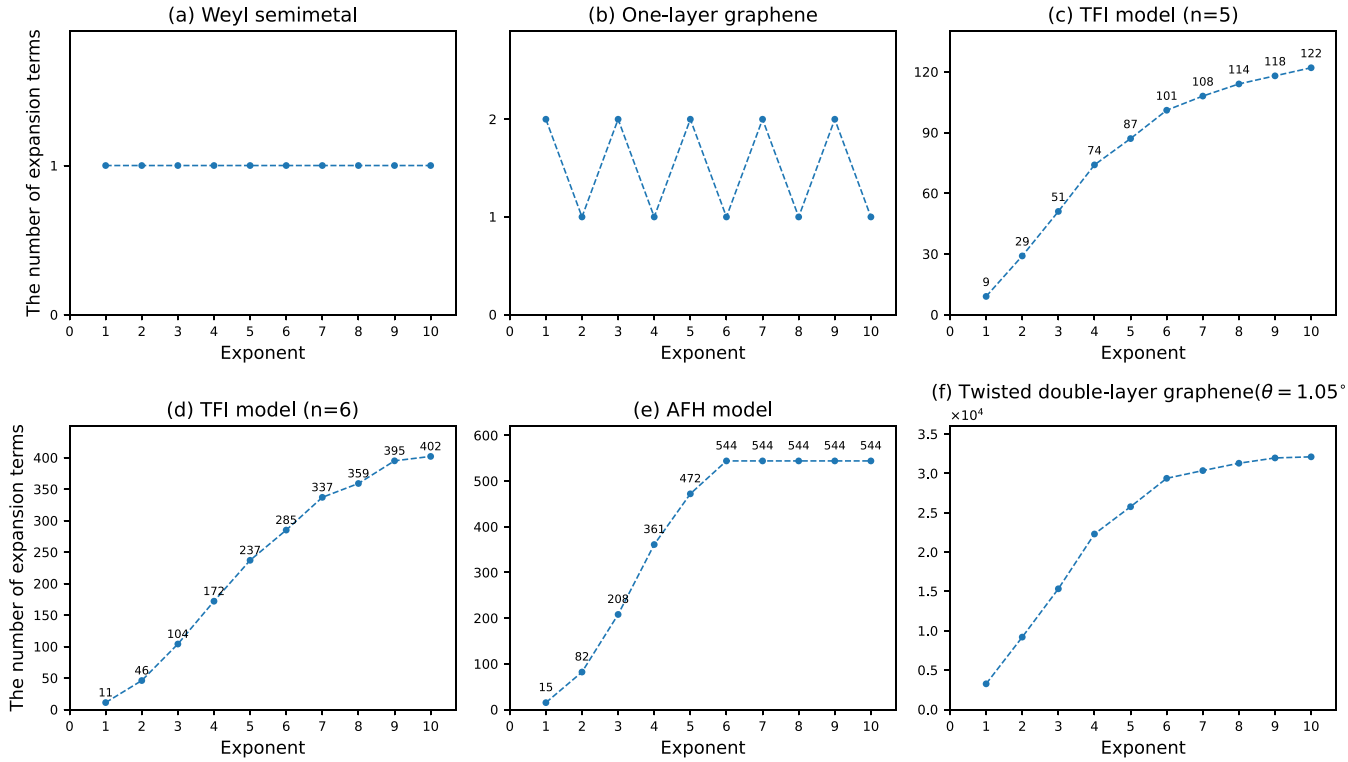

FIG. 10. The relationship between the number of terms in the Pauli expansion and the power of the Hamiltonian. (a) The minimal model for a Weyl semimetal in Eq. (23) and $k_x = k_y = k_z = 0$. (b) The model of one-layer graphene in Eq. (24) and $kx = ky = 2\pi$. (c) and (d) The 1D transverse-field Ising (TFI) models with five sites, $h = 2$, and six sites, $h = 1$ respectively. (e) The 1D antiferromagnetic Heisenberg (AFH) model with six sites. (f) The model of twisted double-layer graphene with $k_x = 0$, $k_y = 0$ for a twist angle of 1.05°. The size of the Hamiltonian matrix is 196×196, while for a Hermitian matrix of the same dimension, the number of terms in the Pauli expansion can be 4^8 at most.

superconducting computers, to validate the effectiveness and feasibility of the P-FQE algorithm. In the future, we will try to find the optimal balance between the number of powers and algorithm complexity to increase the efficiency of our algorithm. Furthermore, we will try to establish a more precise relationship between the power of Hamiltonians for various physical systems and the number of terms in their expansion using a linear combination of unitary operators.

ACKNOWLEDGMENTS

We gratefully acknowledge the support from the National Natural Science Foundation of China under Grant No. 12005015, the Beijing Nova Program under Grant No. 20230484345, and Beijing Advanced Innovation Center for Future Chip (ICFC). We also gratefully acknowledge support from the Extreme Condition User Facility in Beijing and Quafu cloud platform for quantum computation.

APPENDIX A: ERROR ESTIMATION AND THE POWER ESTIMATION

In Sec. II B 1, we denote $\frac{A^t x^{(0)}}{\sqrt{x^{(0)\dagger} A^{2t} x^{(0)}}} = |x^{(t)}\rangle$. Then the error ϵ can be estimated,

$$\begin{aligned}\epsilon &= \langle x^{(t)}|A|x^{(t)}\rangle - \lambda_0 \\ &= \frac{\sum_{i=0}^{n-1} a_i^2 \lambda_i^{2t+1}}{\sum_{i=0}^{n-1} a_i^2 \lambda_i^{2t}} - \lambda_0 \\ &= \frac{\sum_{i=1}^{n-1} a_i^2 \lambda_0^{2t} \left(\frac{\lambda_i}{\lambda_0}\right)^{2t} (\lambda_i - \lambda_0)}{\sum_{i=0}^{n-1} a_i^2 \lambda_0^{2t} \left(\frac{\lambda_i}{\lambda_0}\right)^{2t}} \\ &= \frac{\sum_{i=1}^{n-1} a_i^2 \left(\frac{\lambda_i}{\lambda_0}\right)^{2t} (\lambda_i - \lambda_0)}{a_0^2 + \sum_{i=1}^{n-1} a_i^2 \left(\frac{\lambda_i}{\lambda_0}\right)^{2t}} \\ &\leqslant \frac{(n-1)a_m^2}{a_0^2} (\lambda_n - \lambda_0) \left(\frac{\lambda_1}{\lambda_0}\right)^{2t}. \end{aligned} \tag{A1}$$

The error decreases exponentially with $2t$ (twice the exponent). That means if we aim to achieve a preset precision ϵ, the value of the exponent needs to be $t = O(\log \frac{n}{\epsilon})$.

APPENDIX B: RELATIONSHIP OF THE NUMBER OF TERMS IN THE PAULI EXPANSION AND THE POWER OF THE HAMILTONIAN

Figure 10 illustrates the relationship between the number of terms in the Pauli expansion and the exponent of the power of the Hamiltonian for six different Hamiltonian models. Model (a) is the minimal model for a Weyl semimetal in Eq. (23). With $k_x = k_y = 0$, the Hamiltonian simplifies to include only the Pauli Z term. Raising the Pauli Z to any power yields either the identity or the Pauli Z operator, thus maintaining the number of terms. Model (b) is the model of one-layer graphene in Eq. (24) and $kx = ky = 2\pi$. The Hamiltonian includes components involving Pauli-X and Pauli-Y terms, with

their exponentiation resulting in either the identity operator or a combination of Pauli-X and Pauli-Y terms.

We also consider the transverse-field Ising (TFI) model and the antiferromagnetic Heisenberg (AFH) model [72]. Model (c) and model (d) are 1D TFI models, with their Hamiltonian forms

$$H_{\mathrm{TFI}} = -h\sum_i X_i - \sum_i Z_i Z_{i+1}. \tag{B1}$$

We consider five sites and set $h = 2$ in model (c), while we consider six sites and $h = 1$ in model (d). Theoretically, they can each have a maximum of $4^5 = 1024$ and $4^6 = 4096$ expansion terms after exponentiation, respectively.

Model (e) is the 1D AFH model with six sites, and its Hamiltonian is

$$H_{\mathrm{AFH}} = \sum_i X_i X_{i+1} + Y_i Y_{i+1} + Z_i Z_{i+1}. \tag{B2}$$

It can be observed in the figure that the number of expansion terms stabilized at 544 after exponentiation, which is significantly fewer than the potential 4096. For models (c), (d), and (e), the number of expansion terms does not significantly increase with increasing powers, and it may even stabilize at a considerably lower count than the theoretical prediction. This phenomenon could be attributed to cancellations occurring among the expansion terms during exponentiation.

For model (f), we consider twisted double-layer graphene with $k_x = 0$ and $k_y = 0$ for a twist angle of 1.05°. Terms with coefficients smaller than 10^{-3} are neglected after expansion. We can always disregard terms with coefficients substantially smaller than others, thereby significantly reducing the number of expansion terms and simplifying the exponentiation process.

From the figure, we observe three scenarios: rapid convergence, fluctuation, or a slow increase in the number of terms in the Pauli expansion with increasing powers of the Hamiltonian. These scenarios are often applicable to other physical systems as well.

APPENDIX C: ANOTHER CIRCUIT UPDATING METHOD

Considering a Hamiltonian $H = \sum_{i=1}^{M} \alpha_i P_i$ (P_i is Pauli word), which has n eigenvalues $\{\lambda_i\}_{i=1}^{n}$ and corresponding orthogonal eigenstates $\{|\psi_i\rangle\}_{i=1}^{n}$. Then any quantum state within the same Hilbert space can be expressed as a linear combination of these eigenstates: $|\Psi\rangle = \sum_{i=1}^{n} a_i|\psi_i\rangle$. We have

$$\begin{aligned}
&\big(H^t - \lambda_1^t|\psi_1\rangle\langle\psi_1|\big)|\Psi\rangle \\
&\quad = \big(H^t - \lambda_1^t|\psi_1\rangle\langle\psi_1|\big)(a_1|\psi_1\rangle + a_2|\psi_2\rangle + \cdots a_n|\psi_n\rangle) \\
&\quad = \big(a_1\lambda_1^t|\psi_1\rangle - a_1\lambda_1^t|\psi_1\rangle\big) + a_2\lambda_2^t|\psi_2\rangle + \cdots + a_n\lambda_n^t|\psi_n\rangle \\
&\quad = \lambda_2^t\left[a_2|\psi_2\rangle + \sum_{i=2}^{n} a_i\left(\frac{\lambda_i}{\lambda_2}\right)^t|\psi_i\rangle\right].
\end{aligned} \tag{C1}$$

When the absolute values of the eigenvalues satisfy the inequality constraint $|\lambda_1| \geqslant |\lambda_2| \geqslant |\lambda_3| \cdots \geqslant |\lambda_n|$, then

$$\lim_{t\to\infty}\left(\frac{\lambda_i}{\lambda_2}\right)^t = 0. \tag{C2}$$

That is, when the exponent t is sufficiently large, we will obtain the first excited state of the Hamiltonian. $(H^t - \lambda_1^t|\psi_1\rangle\langle\psi_1|)|\Psi\rangle$ has the same result as $(H - \lambda_1|\psi_1\rangle\langle\psi_1|)^t|\Psi\rangle$, which is illustrated in Sec. II B. λ_1 and the Pauli expansion of $|\psi_1\rangle\langle\psi_1|$ can be obtained from Pauli measurement as described in Sec. II C. The quantum circuit operator required to calculate the jth excited state is

$$\begin{aligned}
U_j &= H^t - \widetilde{\lambda_1}^t|\widetilde{\psi_1}\rangle\langle\widetilde{\psi_1}| - \widetilde{\lambda_2}^t|\widetilde{\psi_2}\rangle\langle\widetilde{\psi_2}| - \cdots \\
&\quad - \widetilde{\lambda_{j-1}}^t|\widetilde{\psi_{j-1}}\rangle\langle\widetilde{\psi_{j-1}}| \\
&= U_{j-1} - \widetilde{\lambda_{j-1}}^t|\widetilde{\psi_{j-1}}\rangle\langle\widetilde{\psi_{j-1}}| \\
&= \sum_{i=1}^{L_j}\beta_i^{(j)}P_i.
\end{aligned} \tag{C3}$$

Compared to the circuit updating method described in Sec. II C, this method eliminates the need for operator exponentiation when constructing quantum circuit operators for computing excited states, further reducing algorithmic complexity. We present the P-FQE algorithm using this circuit updating method in Algorithm 1.

ALGORITHM 1. The P-FQE algorithm.

Input: Hamiltonian $H = \sum_{i=1}^{M}\alpha_i P_i$, State $|\Psi_0\rangle$, Exponent t, The highest energy level needed to be determined: J
Output: Eigenvalues $\{\widetilde{\lambda_i}\}_{i=1}^{J}$, Eigenstates $\{|\widetilde{\psi_i}\rangle\}_{i=1}^{J}$
1: Pauli expansion of the power of the Hamiltonian: $U_1 = H^t = \sum_{i=1}^{L_1}\beta_i^{(1)}P_i$
2: **while** $j \leqslant J$ **do**
3: Apply circuit once to $|\Psi_0\rangle$, having $|\widetilde{\psi_j}\rangle = U_j|\Psi_0\rangle$;
4: Pauli measure $\varepsilon_i^{(j)} = \langle\widetilde{\psi_j}|P_i|\widetilde{\psi_j}\rangle$;
5: return $\widetilde{\lambda_j} = \sum_{i=1}^{M}\alpha_i\varepsilon_i^{(j)}$, $|\widetilde{\psi_j}\rangle\langle\widetilde{\psi_j}| = \sum_{i=1}^{L_j}\frac{\varepsilon_i^{(j)}}{2^n}P_i$;
6: Reconstruct circuit $U_{j+1} = U_j - \widetilde{\lambda_j}^t|\widetilde{\psi_j}\rangle\langle\widetilde{\psi_j}| = \sum_{i=1}^{L_{j+1}}\beta_i^{(j+1)}P_i$
7: **end while**

APPENDIX D: A SUPPLEMENT OF NUMERICAL SIMULATION

We examined double-layer graphene models at twist angles of 0.5°, 1.05°, and 5°, respectively, using two k-points as an example. For each of these six models, we assessed the convergence of the first 10, 30, and 60 energy levels as the exponent of the power of operators increased using our method. As we can see in Fig. 11, convergence becomes slower with higher energy levels, as solving for higher energy levels requires prior solutions for all preceding energy levels.

We also calculated the corresponding fidelity or average error, which decreases as the exponent increases, as shown in Fig. 12. For the twisted double-layer graphene models at three different twist angles, we focused on the simulation

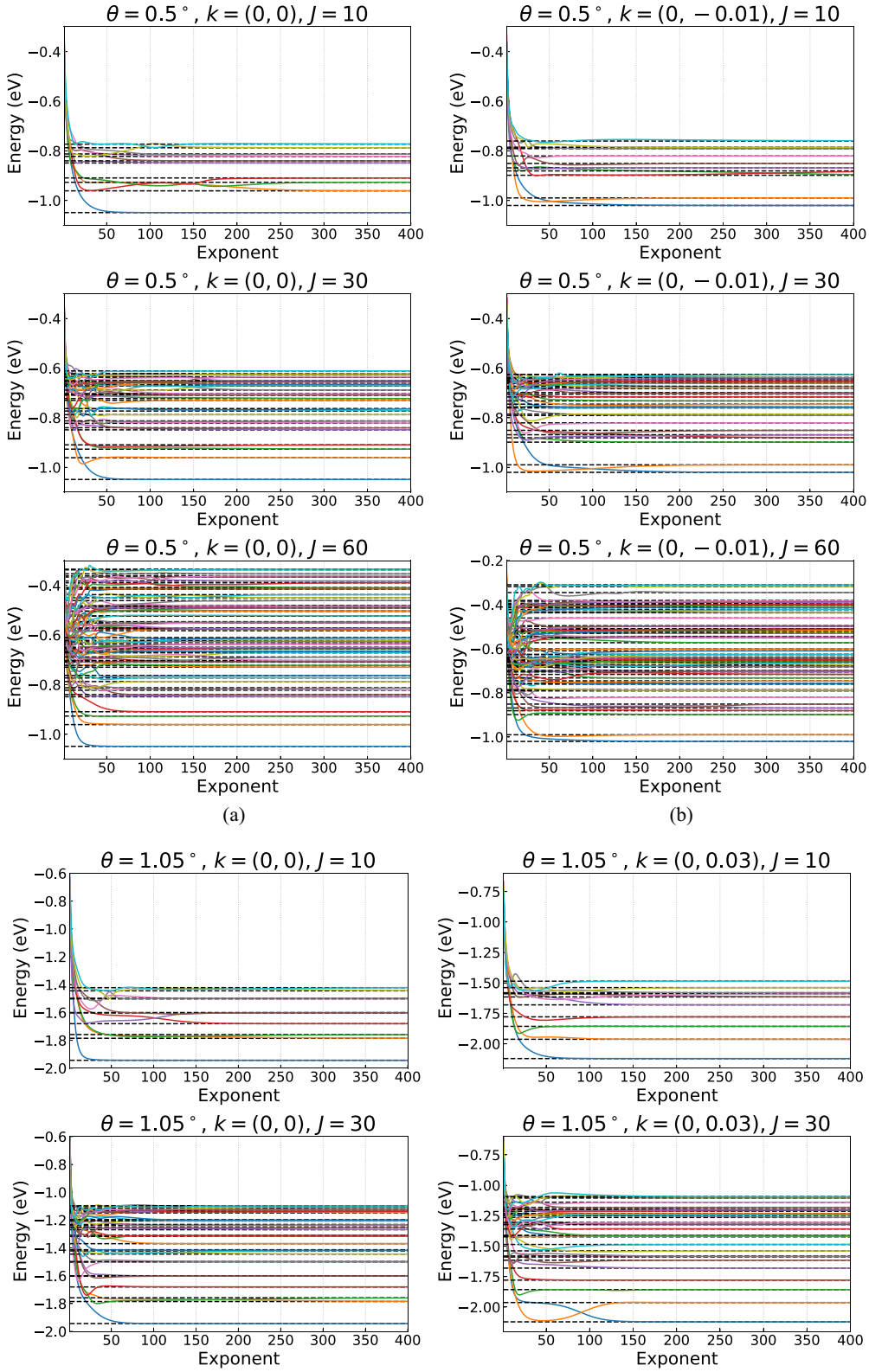

FIG. 11. Convergence with the power of the Hamiltonian. The horizontal lines represent the theoretical values. With a sufficient value of the exponent, the simulated values will converge to the theoretical values.

error at $k = (0, 0)$ for a demonstration. The formula employed for computing the average error is $(\sum_1^J \frac{|E_{\text{simu}} - E_{\text{theo}}|}{E_{\text{theo}}})/J$, where E_{simu} denotes the simulation value and E_{theo} represents the theoretical value, respectively.

As shown in Fig. 12, for a twist angle of 1.05° and $k = (0, 0)$, if we want the average error of the first 60 energy levels to be less than 0.1, we just need less than 40th power. If we want the average error of the first 10 energy levels to be less

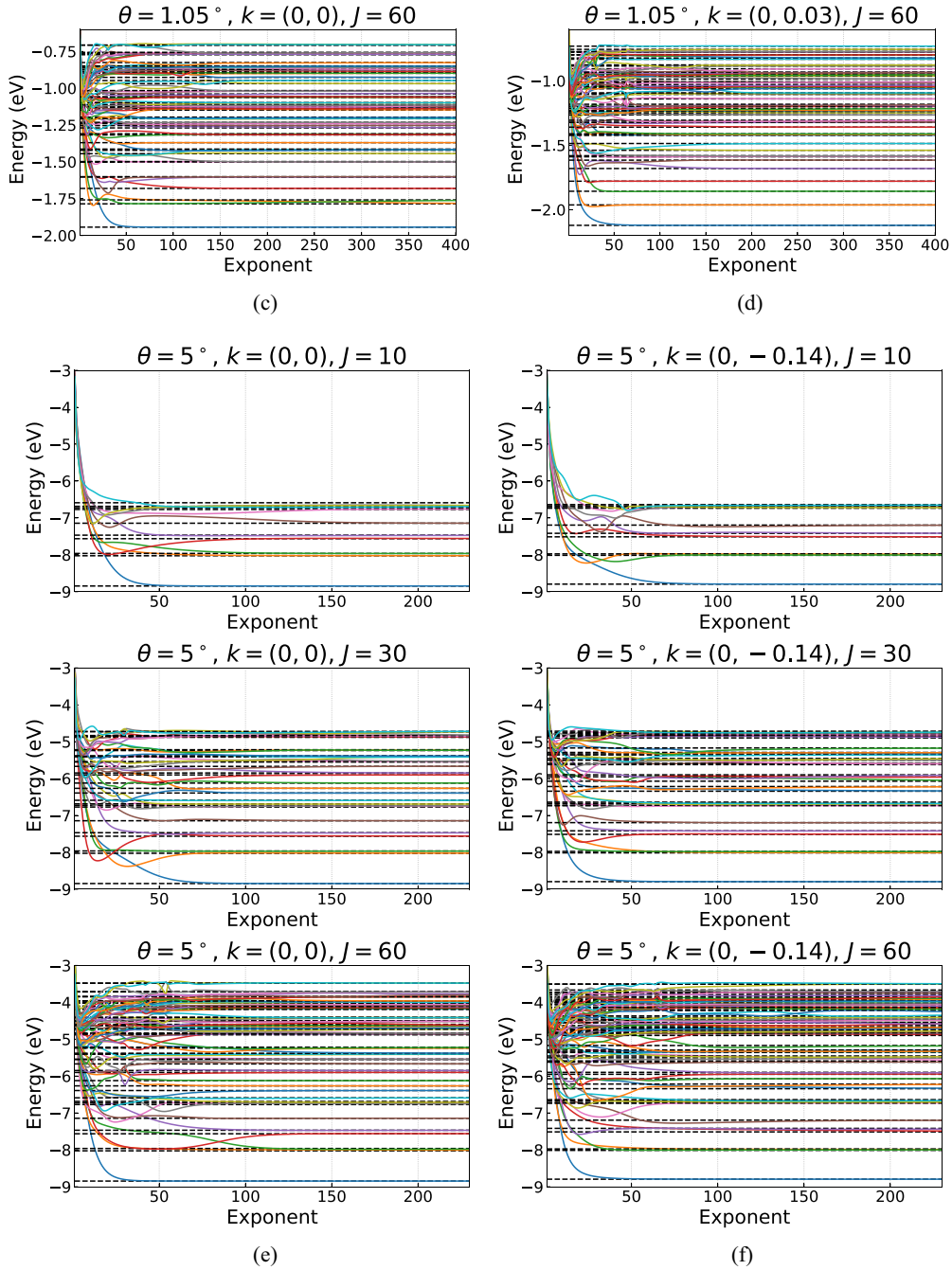

FIG. 11. (*Continued.*)

than 0.01, we need less than 100th power. And if we want the average error of the first 60 energy levels to be less than 0.01, we need about 300th power. When it comes to solving for more energy levels, more power is needed to meet this precision requirement. For convenience, we directly took the 400th power of the Hamiltonian in the main text. And the analysis of the other two double-layer graphene models at twist angles of 0.5° and 5° is similar. However, in practical applications, we can certainly use less power of the Hamiltonian at lower energy levels and gradually increase the power as we continue solving for higher energy levels.

APPENDIX E: QUAFU QUANTUM CLOUD PLATFORM AND IBM QUANTUM

Quafu is an open quantum computing cloud platform [67], connected to a 136-qubit quantum computer and two other 18- and 10-qubit superconducting quantum computers. In the experiment of Weyl semimetal, we use the first two qubits of the 18-qubit processor called ScQ-P18, with an idle qubit frequency of 4.590 and 5.016 GHz, and up to 97.5% average fidelity of CZ gates. The device parameters are listed in Table I.

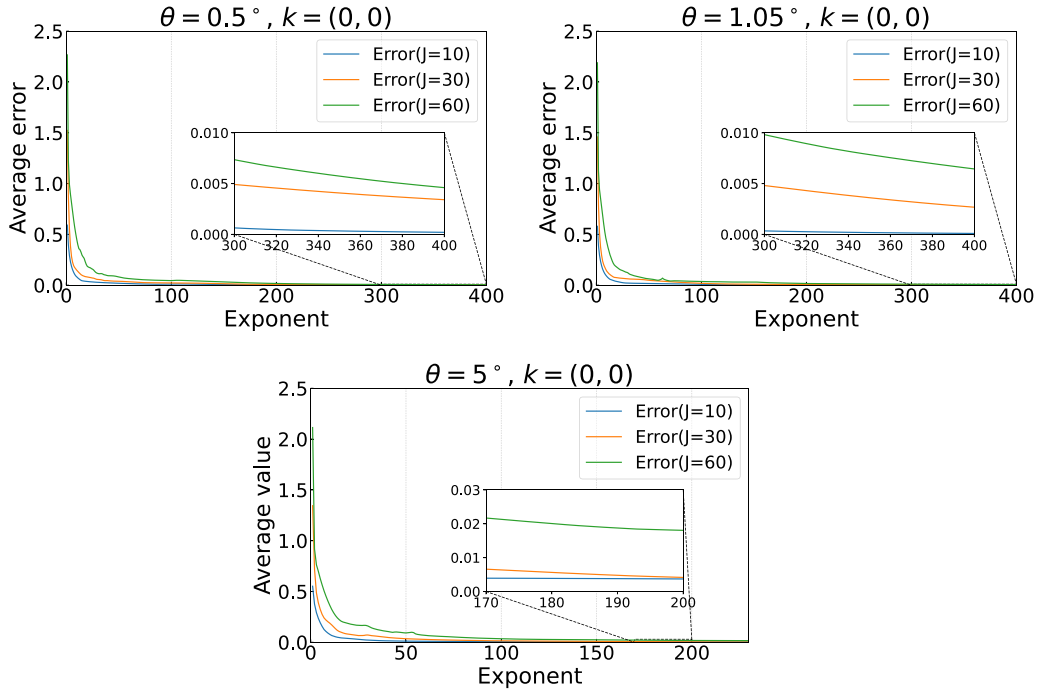

FIG. 12. The average error of simulation. At a specific k-point (0,0), the average error for the first J energy levels is calculated when performing numerical simulations using P-FQE.

In the experiment to compute the energy band of graphene, we selected the quantum backend ibm_nairobi on the IBM quantum cloud platform, a superconducting quantum chip with seven qubits. The basis gates of ibm_nairobi are CX, ID, RZ, SX, and X, and the median errors for the CNOT gate, SX gate, and readout are 9.360×10^{-3}, 2.894×10^{-4}, and 2.500×10^{-2}. The first three qubits are used in our circuits, with work frequencies of 5.26, 5.17, and 5.274 GHz. The topological maps of ScQ-P18 and ibm_nairobi are shown in Fig. 13.

TABLE I. Device parameters. $T1$ and $T2$ represent the decoherence time of the qubit energy and the qubit phase. η corresponds to the anharmonicity of the qubit. ω^i represents the idle frequency of the qubit. ω^r corresponds to the resonant frequency of the qubit during readout. T_{CZ} represents the CZ (controlled-Z) gate duration. Connection shows the connected two qubits that form the CZ gate. F_{CZ} represents the fidelity of the CZ gate formed by the connected qubits, which is obtained by randomized benchmarking. $F0$ and $F1$ are the readout fidelity of the qubit in $|0\rangle$ and $|1\rangle$.

Qubit	$T1$ (μs)	$T2$ (μs)	$\eta/2\pi$ (GHz)	$\omega^i/2\pi$ (GHz)	$\omega^r/2\pi$ (GHz)	T_{CZ} (μs)	Connection	F_{CZ}	$F0$	$F1$
Q0	57.564	4.239	0.205	4.590	6.776	30	Q1-Q0	0.975	0.953	0.853
Q1	27.885	3.699	0.192	5.016	6.760	30	Q2-Q1	0.909	0.978	0.905
Q2	41.442	4.835	0.203	4.620	6.737	30	Q3-Q2	0.964		
Q3	40.102	2.299	0.198	4.965	6.713	30	Q4-Q3	0.951		
Q4	28.994	5.690	0.205	4.542	6.693	30	Q5-Q4	0.945		
Q5	23.602	2.203	0.194	5.030	6.676	30	Q6-Q5	0.954		
Q6	26.839	3.420	0.204	4.615	6.650	30	Q7-Q6	0.964		
Q7	19.760	2.438	0.200	5.000	6.634	30	Q8-Q7	0.969		
Q8	23.219	3.534	0.206	4.640	6.625	30	Q9-Q8	0.962		
Q9	27.308	1.325	0.200	5.056	6.648	30	Q10-Q9	0.962		
Q10	41.155	2.779	0.205	4.685	6.665	30	Q11-Q10			
Q11	28.119	1.494	0.198	4.993	6.693	30				
Q12	45.117	2.953	0.206	4.509	6.705	30				
Q13	29.795	1.568	0.198	4.869	6.725	30				
Q14	45.117	5.467	0.204	4.578	6.751	30				
Q15	37.279	3.068	0.196	5.048	6.771	30				
Q16	40.837	5.153	0.203	4.682	6.788	30				
Q17	41.428	3.116	0.197	5.125	6.807	30				

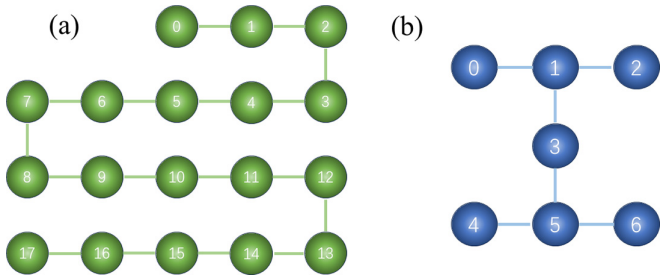

FIG. 13. The topological maps of superconducting quantum chips ScQ-P18 and ibm_nairobi. Each qubit is coupled with its nearest neighbors. (a) The topological map of backend ScQ-P18 on Quafu. (b) The topological map of backend ibm_nairobi on IBM Quantum.

APPENDIX F: EXPERIMENTAL DATA

Tables II and III are the results of experiments conducted on two superconducting quantum computers. The error is calculated by (average value − theoretical value)/theoretical value, where the average value is the average of three trial results. The Hamiltonian of the Weyl semimetal used in experiments only involves the Pauli-Z term. Therefore, we only need to perform Pauli-Z measurement, which reduces errors in principle. For the Quafu platform, we implemented a readout correction for the superconducting quantum hardware. We denote the probability of reading out qubit Q_j in $|0\rangle$ ($|1\rangle$) when it is prepared in a $|0\rangle$ ($|1\rangle$) state as F_0^j and F_1^j, respectively. The readout correction matrix of Q_j can be written as

$$M_j = \begin{pmatrix} F_0^j & 1-F_1^j \\ 1-F_0^j & -F_1^j \end{pmatrix}. \tag{F1}$$

After applying M_j^{-1} to the final state $|\phi_j\rangle$, we obtain $|\psi_j\rangle$. We take $|\psi_j\rangle$ as the readout result, which helps to further reduce errors. As a result, some of our experimental results indicate zero errors.

TABLE II. The experimental results of Weyl semimetal on the Quafu quantum cloud platform using an 18-qubit chip (ScQ-P18).

k-point ($k_x = k_y = 0$)	Energy level n	Trial 1 (eV)	Trial 2 (eV)	Trial 3 (eV)	Average value (eV)	Theoretical value (eV)	Error (%)
$k_z = -1.4$	$n = 1$	−0.9328	−0.9600	−0.9398	−0.9442	−0.9600	−1.645
	$n = 2$	0.9600	0.9600	0.9600	0.9600	0.9600	0.000
$k_z = -0.6$	$n = 1$	−0.6400	−0.6400	−0.6400	−0.6400	−0.6400	0.000
	$n = 2$	0.5647	0.6400	0.6211	0.6086	0.6400	−4.910
$k_z = 0$	$n = 1$	−1.0000	−1.0000	−1.0000	−1.0000	−1.0000	0.000
	$n = 2$	0.8935	0.9159	0.9806	0.9300	1.0000	−6.999
$k_z = 0.7$	$n = 1$	−0.5100	−0.5100	−0.5100	−0.5100	−0.5100	0.000
	$n = 2$	0.4567	0.5100	0.5041	0.4903	0.5100	3.872
$k_z = 1.3$	$n = 1$	−0.6900	−0.6877	−0.6821	−0.6866	−0.6900	−0.491
	$n = 2$	0.6900	0.6900	0.6900	0.6900	0.6900	0.000
$k_z = 2$	$n = 1$	−2.7315	−3.0000	−2.9241	−2.8852	−3.0000	−3.827
	$n = 2$	2.9787	3.0000	3.0000	2.9929	3.0000	0.237

TABLE III. The experimental results of single-layer graphene on the IBM Quantum using the chip ibm_nairobi.

k-point (k_x, k_y)	Energy level n	Trial 1 (eV)	Trial 2 (eV)	Trial 3 (eV)	Average value (eV)	Theoretical value (eV)	Error (%)
$(\frac{\sqrt{3}\pi}{9a}, \frac{\pi}{3a})$	$n = 1$	−1.5886	−1.6339	−1.6324	−1.6183	−2.0000	−19.080
	$n = 2$	1.7945	1.8008	1.8040	1.7998	2.0000	−10.010
(0,0)	$n = 1$	−2.4149	−2.4513	−2.4221	−2.4294	−3.0000	−19.019
	$n = 2$	2.6940	2.7135	2.7079	2.7051	3.0000	−9.829
$(0, \frac{3\pi}{18a})$	$n = 1$	−2.0679	−2.1165	−2.0137	−2.0660	−2.7979	−26.158
	$n = 2$	2.1502	2.1970	2.0870	2.1447	2.7979	−23.345
$(0, \frac{\pi}{3a})$	$n = 1$	−1.6400	−1.5467	−1.6052	−1.5973	−2.2361	−28.568
	$n = 2$	1.6833	1.7637	1.7509	1.7326	2.2361	−22.515
$(0, \frac{\pi}{2a})$	$n = 1$	−1.0591	−1.0491	−1.1572	−1.0885	−1.4736	−26.136
	$n = 2$	1.1220	1.1112	1.0810	1.1047	1.4763	−25.170
$(0, \frac{2\pi}{3a})$	$n = 1$	−0.7552	−0.7755	−0.7557	−0.7621	−1.0000	−23.786
	$n = 2$	0.7357	0.7791	0.7635	0.7594	1.0000	−24.057
$(\frac{\sqrt{3}\pi}{9a}, \frac{2\pi}{3a})$	$n = 1$	−0.5303	−0.5332	−0.5230	−0.5288	−0.7321	−27.767
	$n = 2$	0.5662	0.5308	0.5206	0.5392	0.7321	−26.348

[1] R. P. Feynman, Int. J. Theor. Phys. **21**, 467 (1982).
[2] P. Benioff, J. Stat. Phys. **22**, 563 (1980).
[3] A. Montanaro, npj Quantum Inf. **2**, 15023 (2016).
[4] K. Bharti, A. Cervera-Lierta, T. H. Kyaw, T. Haug, S. Alperin-Lea, A. Anand, M. Degroote, H. Heimonen, J. S. Kottmann, T. Menke *et al.*, Rev. Mod. Phys. **94**, 015004 (2022).
[5] P. W. Shor, SIAM Rev. **41**, 303 (1999).
[6] S. Lloyd, Science **273**, 1073 (1996).
[7] A. W. Harrow, A. Hassidim, and S. Lloyd, Phys. Rev. Lett. **103**, 150502 (2009).
[8] B. Yan, Z. Tan, S. Wei, H. Jiang, W. Wang, H. Wang, L. Luo, Q. Duan, Y. Liu, W. Shi *et al.*, arXiv:2212.12372.
[9] Z. Wang, S. Wei, G.-L. Long, and L. Hanzo, Sci. China Inf. Sci. **65**, 200503 (2022).
[10] S.-J. Wei, C. Wei, P. Lv, C. Shao, P. Gao, Z. Zhou, K. Li, T. Xin, and G.-L. Long, Sci. Bull. **68**, 494 (2023).
[11] E. F. Dumitrescu, A. J. McCaskey, G. Hagen, G. R. Jansen, T. D. Morris, T. Papenbrock, R. C. Pooser, D. J. Dean, and P. Lougovski, Phys. Rev. Lett. **120**, 210501 (2018).
[12] A. Kandala, A. Mezzacapo, K. Temme, M. Takita, M. Brink, J. M. Chow, and J. M. Gambetta, Nature (London) **549**, 242 (2017).
[13] A. Aspuru-Guzik, A. D. Dutoi, P. J. Love, and M. Head-Gordon, Science **309**, 1704 (2005).
[14] Y. Nam, J.-S. Chen, N. C. Pisenti, K. Wright, C. Delaney, D. Maslov, K. R. Brown, S. Allen, J. M. Amini, J. Apisdorf *et al.*, npj Quantum Inf. **6**, 33 (2020).
[15] P. Lv, S. Wei, H.-N. Xie, and G. Long, Sci. China Phys. Mech. Astron. **66**, 240311 (2023).
[16] F. Bloch, Z. Phys. **52**, 555 (1929).
[17] A. H. Wilson, Proc. R. Soc. Lond. A **133**, 458 (1931).
[18] A. Peruzzo, J. McClean, P. Shadbolt, M.-H. Yung, X.-Q. Zhou, P. J. Love, A. Aspuru-Guzik, and J. L. O'brien, Nat. Commun. **5**, 4213 (2014).
[19] M. Cerezo, A. Arrasmith, R. Babbush, S. C. Benjamin, S. Endo, K. Fujii, J. R. McClean, K. Mitarai, X. Yuan, L. Cincio *et al.*, Nat. Rev. Phys. **3**, 625 (2021).
[20] F. T. Cerasoli, K. Sherbert, J. Sławińska, and M. B. Nardelli, Phys. Chem. Chem. Phys. **22**, 21816 (2020).
[21] N. Yoshioka, T. Sato, Y. O. Nakagawa, Y.-Y. Ohnishi, and W. Mizukami, Phys. Rev. Res. **4**, 013052 (2022).
[22] T. Jones, S. Endo, S. McArdle, X. Yuan, and S. C. Benjamin, Phys. Rev. A **99**, 062304 (2019).
[23] O. Higgott, D. Wang, and S. Brierley, Quantum **3**, 156 (2019).
[24] J. Wen, D. Lv, M.-H. Yung, and G.-L. Long, Quantum Eng. **3**, e80 (2021).
[25] K. M. Nakanishi, K. Mitarai, and K. Fujii, Phys. Rev. Res. **1**, 033062 (2019).
[26] R. M. Parrish, E. G. Hohenstein, P. L. McMahon, and T. J. Martínez, Phys. Rev. Lett. **122**, 230401 (2019).
[27] J. Preskill, Quantum **2**, 79 (2018).
[28] J. R. McClean, S. Boixo, V. N. Smelyanskiy, R. Babbush, and H. Neven, Nat. Commun. **9**, 4812 (2018).
[29] L. Bittel and M. Kliesch, Phys. Rev. Lett. **127**, 120502 (2021).
[30] B. Barak and K. Marwaha, arXiv:2106.05900.
[31] S. Wei, H. Li, and G. Long, Research **2020**, 1486935 (2020).
[32] J. Wen, Z. Wang, C. Chen, J. Xiao, H. Li, L. Qian, Z. Huang, H. Fan, S. Wei, and G. Long, Quantum **8**, 1219 (2024).
[33] J. T. Seeley, M. J. Richard, and P. J. Love, J. Chem. Phys. **137**, 224109 (2012).
[34] C. D. Batista and G. Ortiz, Phys. Rev. Lett. **86**, 1082 (2001).
[35] M. Panju, arXiv:1105.1185.
[36] L. Gui-Lu, Commun. Theor. Phys. **45**, 825 (2006).
[37] L. Gui-Lu and L. Yang, Commun. Theor. Phys. **50**, 1303 (2008).
[38] L. Gui-Lu, L. Yang, and W. Chuan, Commun. Theor. Phys. **51**, 65 (2009).
[39] A. M. Childs and N. Wiebe, Quantum Inf. Comput. **12**, 901 (2012).
[40] J. Wen, C. Zheng, X. Kong, S. Wei, T. Xin, and G. Long, Phys. Rev. A **99**, 062122 (2019).
[41] J. Wen, G. Qin, C. Zheng, S. Wei, X. Kong, T. Xin, and G. Long, npj Quantum Inf. **6**, 28 (2020).
[42] J. Wen, C. Zheng, Z. Ye, T. Xin, and G. Long, Phys. Rev. Res. **3**, 013256 (2021).
[43] R. Sarkar and E. van den Berg, Res. Math. Sci. **8**, 14 (2021).
[44] M. Kummer, Ind. Univ. Math. J. **30**, 281 (1981).
[45] E. Wigner, Phys. Rev. **51**, 106 (1937).
[46] M. Lax, *Symmetry Principles in Solid State and Molecular Physics* (Dover Publications, New York, 2001).
[47] E. Koridon, S. Yalouz, B. Senjean, F. Buda, T. E. O'Brien, and L. Visscher, Phys. Rev. Res. **3**, 033127 (2021).
[48] J. Lee, D. W. Berry, C. Gidney, W. J. Huggins, J. R. McClean, N. Wiebe, and R. Babbush, PRX Quantum **2**, 030305 (2021).
[49] T. Ozaki, Phys. Rev. B **67**, 155108 (2003).
[50] J. C. Phillips and L. Kleinman, Phys. Rev. **116**, 287 (1959).
[51] V. Giovannetti, S. Lloyd, and L. Maccone, Phys. Rev. Lett. **100**, 160501 (2008).
[52] P. Rebentrost, M. Schuld, L. Wossnig, F. Petruccione, and S. Lloyd, New J. Phys. **21**, 073023 (2019).
[53] G.-L. Long and Y. Sun, Phys. Rev. A **64**, 014303 (2001).
[54] T. Xin, S.-J. Wei, J. S. Pedernales, E. Solano, and G.-L. Long, Phys. Rev. A **96**, 062303 (2017).
[55] S.-J. Wei, T. Xin, and G.-L. Long, Sci. China Phys. Mech. Astron. **61**, 1 (2018).
[56] G. Brassard, P. Hoyer, M. Mosca, and A. Tapp, Contemp. Math. **305**, 53 (2002).
[57] D. W. Berry, A. M. Childs, R. Cleve, R. Kothari, and R. D. Somma, Phys. Rev. Lett. **114**, 090502 (2015).
[58] O. K. Andersen and O. Jepsen, Phys. Rev. Lett. **53**, 2571 (1984).
[59] C. Goringe, D. Bowler, and E. Hernandez, Rep. Prog. Phys. **60**, 1447 (1997).
[60] R. Bistritzer and A. H. MacDonald, Proc. Natl. Acad. Sci. USA **108**, 12233 (2011).
[61] G. Oster, M. Wasserman, and C. Zwerling, J. Opt. Soc. Am. **54**, 169 (1964).
[62] N. P. Armitage, E. J. Mele, and A. Vishwanath, Rev. Mod. Phys. **90**, 015001 (2018).
[63] C. M. Wang, H.-P. Sun, H.-Z. Lu, and X. C. Xie, Phys. Rev. Lett. **119**, 136806 (2017).
[64] S.-B. Zhang, H.-Z. Lu, and S.-Q. Shen, New J. Phys. **18**, 053039 (2016).
[65] R. Okugawa and S. Murakami, Phys. Rev. B **89**, 235315 (2014).
[66] H.-Z. Lu, S.-B. Zhang, and S.-Q. Shen, Phys. Rev. B **92**, 045203 (2015).

[67] Detailed information about Quafu cloud platform can be found at website, github, and document.
[68] A. K. Geim, Science **324**, 1530 (2009).
[69] X. Li, J. Yu, S. Wageh, A. A. Al-Ghamdi, and J. Xie, Small **12**, 6640 (2016).
[70] D. Abergel, V. Apalkov, J. Berashevich, K. Ziegler, and T. Chakraborty, Adv. Phys. **59**, 261 (2010).
[71] S. Konschuh, M. Gmitra, and J. Fabian, Phys. Rev. B **82**, 245412 (2010).
[72] G. Carleo and M. Troyer, Science **355**, 602 (2017).